



TIME-RESOLVED PENETRATION OF LONG RODS INTO STEEL TARGETS

CHARLES E. ANDERSON, JR,[†] VOLKER HOHLER,[‡]

JAMES D. WALKER[†] and ALOIS J. STILP[‡]

[†]Southwest Research Institute, Engineering and Materials Sciences Division, P.O. Drawer 28510, San Antonio, TX 78228-0510, U.S.A. and [‡]Ernst-Mach-Institut, Terminal Ballistics and Impact Physics Division, Eckerstrasse 4, 78 Freiburg i.Br., Germany

(Received 23 November 1993; in revised form 28 March 1994)

Summary—The penetration behavior of tungsten alloy, long-rod penetrators into high-hard steel is investigated at two impact velocities; 1.25 km/s and 1.70 km/s. The positions of the nose and tail of the projectile were measured by means of a 600 kV flash X-ray system at different times during penetration. The wavecode CTH was used to numerically simulate the experiments. The computational results are in very good agreement with the experimental position–time data. Additionally, the computational model reproduces the qualitative behavior for impact conditions near the ballistic limit.

NOTATION

B	Johnson–Cook constitutive constant
C	Johnson–Cook constitutive constant
D	projectile diameter
G	shear modulus
L, L_0	initial projectile length
L_R	instantaneous (residual) projectile length
m	Johnson–Cook constitutive constant (temperature exponent)
n	Johnson–Cook constitutive constant (work-hardening exponent)
S_H	distance projectile tail has moved
S_K	penetration depth
t	time
T	plate thickness
T_{BL}	ballistic limit thickness
V_{BL}	ballistic limit velocity
V_p	impact velocity
V_r	residual velocity
V_s	striking (impact) velocity
Y_0	Johnson–Cook constitutive constant (initial flow stress)
ϵ_p	equivalent plastic strain
$\dot{\epsilon}_p$	plastic strain rate
ν	Poisson's ratio
σ_{eq}	equivalent stress
σ_{fail}	fracture stress
θ	temperature
θ^*	homologous temperature
θ_m	melt temperature
θ_0	initial temperature

INTRODUCTION

The penetration of metallic targets using numerical simulations has been studied fairly extensively during the past decade; Refs [1,2] supply a reasonably complete summary of articles and papers that have used numerical simulations and analytical formulations to investigate long-rod penetration into steel targets. Typically, the final depth of penetration

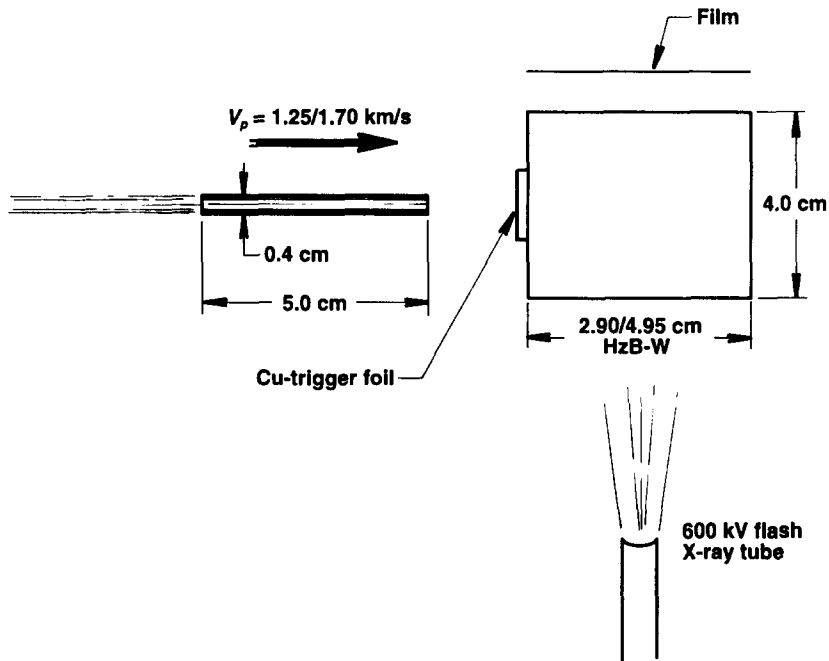


Fig. 1. Schematic of experimental arrangement for steel targets.

provides the only link between experiments and the results of numerical simulations, although occasionally crater diameters are also compared. Flash radiography can be used under certain conditions to determine the positions of the projectile/target interface and the projectile tail, and also the instantaneous length of the projectile, at specific instances of time during the penetration process. Unfortunately, this information is time consuming and expensive to obtain, and the ability to “see” through the target constrains the dimensions of the targets that can be used in the experiments. Numerical simulations of long-rod penetration into steel and titanium targets were compared with a limited set of time-resolved X-ray data in Ref. [3]. Agreement between the numerical simulations and the experimental data was adequate, but certainly could be better. The discrepancies were attributed to the fact that the constitutive behavior of the materials used in the experiments had to be estimated. Since the focus of the work in Ref. [3] was on an examination of the time dependence of the target resistance R_t that is used in the Tate model [4], no attempt was made to determine more accurate constitutive parameters. The present paper describes the results of a considerably larger number of experiments into high-hard steel targets. Constitutive constants have been determined for materials similar to those used in the experiments, so a critical comparison can be made between the numerical simulations and the experimental data.

EXPERIMENTAL PROCEDURES AND RESULTS

The experimental arrangement is depicted in Fig. 1. Blunt-nosed, tungsten-sintered alloy projectiles, 0.40 cm in diameter and 5.0 cm long (length-to-diameter L/D ratio of 12.5), were impacted against the targets at a velocity of 1.25 and 1.70 km/s; the target obliquity was 0° .† The tungsten-sintered alloy had a density of 17.6 g/cm^3 (92.5% W, 4.85% Ni, 2.4% Fe, 0.25% Co) and a yield strength of 1.20 GPa (elongation at failure was 10%); the rods were manufactured by Metallwerk Plansee, Reutte, Austria. The steel targets were high-hard

† The projectiles had a conical-shaped drag cone (0.12 cm long, with a maximum diameter of 0.8 cm at the base of the projectile), made from the same tungsten alloy, press-fitted onto the cylindrical rod. The drag cone added 0.3 g mass to the ideal cylindrical projectile. Previous experience has shown that the influence of this fin on the ballistic limit can be neglected.

Table 1. Impact velocity, pitch and yaw, and final target state for the 2.90 cm thick target

Experiment no.	V_p (km/s)	Pitch/yaw ($^\circ/^\circ$)	Target state
4811	1.260	2.0/0.5	p
4812	1.241	1.2/1.0	np
4816	1.258	1.5/1.5	p/np
4813	1.271	0.8/0.8	p
4817	1.230	1.2/1.0	np
4818	1.229	0.0/1.0	np
4814	1.270	0.3/1.1	p
4819	1.270	0.1/3.0	p
4815	1.251	0.1/0.3	np
4820	1.231	1.0/0.2	np

p = perforation

np = no perforation

p/np = between p and np, which implies ballistic limit.

Table 2. Impact velocity, pitch and yaw, and final target state for the 4.95 cm thick target

Experiment no.	V_p (km/s)	Pitch/yaw ($^\circ/^\circ$)	Target state
4784	1.681	1.5/3.0	np
4790	1.683	1.0/3.8	np
4781	1.679	3.0/0.0	np
4783	1.709	0.0/3.8	p
4788	1.707	3.1/2.3	p/np
4789	1.694	1.5/1.5	p/np
4785	1.680	1.0/2.0	np
4782	1.681	1.5/3.0	np
4786	1.720	0.3/4.0	p
4787	1.712	0.5/2.3	p

armor steel (HzB-W), Vickers hardness 440 ± 20 , with a density of 7.85 g/cm^3 ; the steel was manufactured by Thyssen Stahl AG, Duisburg, Germany. The yield strength was $1.45 \pm 0.1 \text{ GPa}$. The lateral dimensions of the plate were 4.0 cm by 7.0 cm. The plate thicknesses divided by the original projectile lengths (T/L) were 0.58 and 0.99 for the two sets of experiments.

The ballistic limit thickness as a function of the striking velocity was established in a previous study. It was then determined that the ballistic limit thicknesses T_{BL} were 2.90 cm at $1.25 \pm 0.02 \text{ km/s}$, and 4.95 cm at $1.70 \pm 0.02 \text{ km/s}$. Based on the tests reported herein, the error in the ballistic limit velocities can be reduced from $\pm 0.02 \text{ km/s}$ to $\pm 0.01 \text{ km/s}$.

Pictures of the penetration process were taken with a 600 kV flash X-ray, triggered at the moment of impact by a thin copper “shorting” screen. One picture per test was taken; the delay time from the trigger was changed for each test to record the projectile at different penetration positions. The contrast sensitivity of the photographic film restricted the lateral dimensions of the steel targets to 4.0 cm; this constraint dictated the scale size of the experiments. All tests and data analysis were conducted at the Ernst-Mach-Institut (EMI). As depicted in Fig. 1, the thicknesses of the steel of the experiments were the ballistic limit thicknesses.

The impact velocity and the (vertical) pitch and (horizontal) yaw are given in Tables 1 and 2 for the two sets of experiments. The fourth column of the table provides information regarding target perforation. The symbol p means that the target was perforated, i.e. there was a penetration hole completely through the target. The symbol np signifies that the target was not perforated, although small cracks were observed on the rear side of some targets. Finally, there were some experiments where the target was not completely perforated, but there were large cracks at the rear surface; these large cracks are interpreted as the “ideal” ballistic limit damage, and are denoted as p/np.

The positions of the projectile nose and tail S_K and S_H , respectively, defined in Fig. 2, were determined from the X-ray shadowgraph. Additionally, the length of the projectile L_R was independently measured. Because S_K , S_H and L_R are independent measurements, the following expression provides a consistency check on the data:

$$L_0 - L_R = S_H - S_K. \quad (1)$$

The experimental spread in the impact velocities was $\pm 0.020 \text{ km/s}$. The experimental data for S_H and S_K were corrected to exactly 1.25 and 1.70 km/s by a simple proportionality at the measured time, i.e. $(S_H)_{adj} = (V_p/V_{exp})(S_H)_{exp}$ and $(S_K)_{adj} = (V_p/V_{exp})(S_K)_{exp}$ where V_{exp} is the

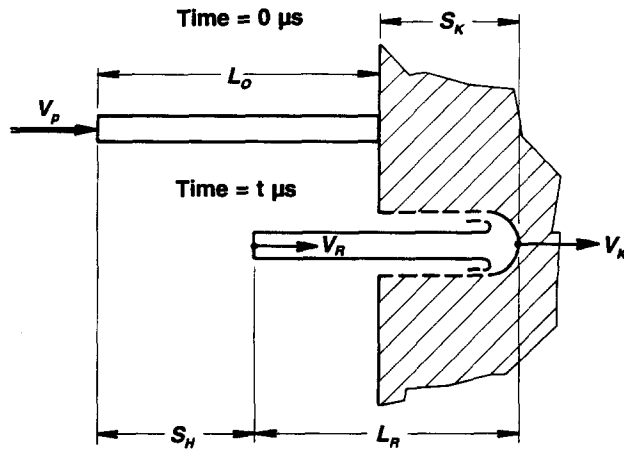


Fig. 2. Nomenclature and measured quantities from flash X-rays.

Table 3. Penetration into high-hard steel:
 $V_p = 1.25$ km/s

Experiment no.	t (μ s)	S_K (cm)	S_H (cm)	L_R (cm)
4811	10.0	0.58	1.19	4.39
4812	19.9	1.08	2.34	3.74
4816	24.9	1.31	2.99	3.32
4813	30.0	1.57	3.49	3.08
4818	34.9	1.66	4.13	2.53
4817	35.0	1.68	4.16	2.52
4814	39.9	2.07	4.61	2.46
4819	44.9	2.13	5.28	1.85
4815	50.0	2.19	5.54	1.65
4820	55.0	2.32	6.33	0.99

Table 4. Penetration into high-hard steel:
 $V_p = 1.70$ km/s

Experiment no.	t (μ s)	S_K (cm)	S_H (cm)	L_R (cm)
4784	10.4	0.92	1.68	4.24
4790	15.3	1.34	2.59	3.75
4781	20.5	1.75	3.46	3.29
4783	20.7	1.72	3.36	3.36
4788	25.3	2.16	4.18	2.98
4789	28.3	2.38	4.69	2.69
4785	30.5	2.62	5.20	2.42
4782	40.4	3.24	6.54–6.74	1.5–1.7
4786	40.6	3.33		
4787	60.3	4.56		

actual (experimental) impact velocity and V_p is 1.25 or 1.70 km/s. No adjustment to the time is performed, i.e. $t = t_{\text{exp}}$. The “corrected” experimental data are given in Tables 3 and 4 for the two impact velocities, respectively.† The position of the projectile tail was not readily discernible in the radiographs taken at late times for the 1.70 km/s experiments. For test number 4782, an estimate was made of the location of the tail position; estimates could not be reliably made for tests 4786 and 4787.

Figures 3(a) and 3(b) are enhanced X-ray shadowgraphs that show the penetrating projectile 20.7 μ s and 25.3 μ s after impact; the depths of penetration are 1.72 and 2.16 cm, respectively. The impact velocity was 1.71 km/s for both tests. The photographs have been positioned in the figure to align the rear of the targets so that the displacement of the projectile is readily evident. The hydrodynamic-like penetration front and the erosion products lining the side of the crater cavity are easily visible in the shadowgraphs.

NUMERICAL SIMULATIONS

The nonlinear, large deformation Eulerian wavecode CTH [5], using the two-dimensional cylindrically symmetric option, was used for the numerical simulations. Although the targets

† The accuracy of the measurements is as follows. The times of the flash X-rays are correct to ± 0.2 μ s (this includes the time interval counter and the short circuit trigger foil). The uncertainty in the impact velocity ΔV_p is $\pm 0.002 V_p$, which is approximately ± 3 m/s for the impact velocities used in these tests. The positions of the nose and tail, measured from the flash X-ray pictures, are accurate to ± 0.01 cm; the uncertainty in the position of the target surface is also ± 0.01 cm. This leads to an uncertainty in S_K , S_H and L_R of ± 0.02 cm.

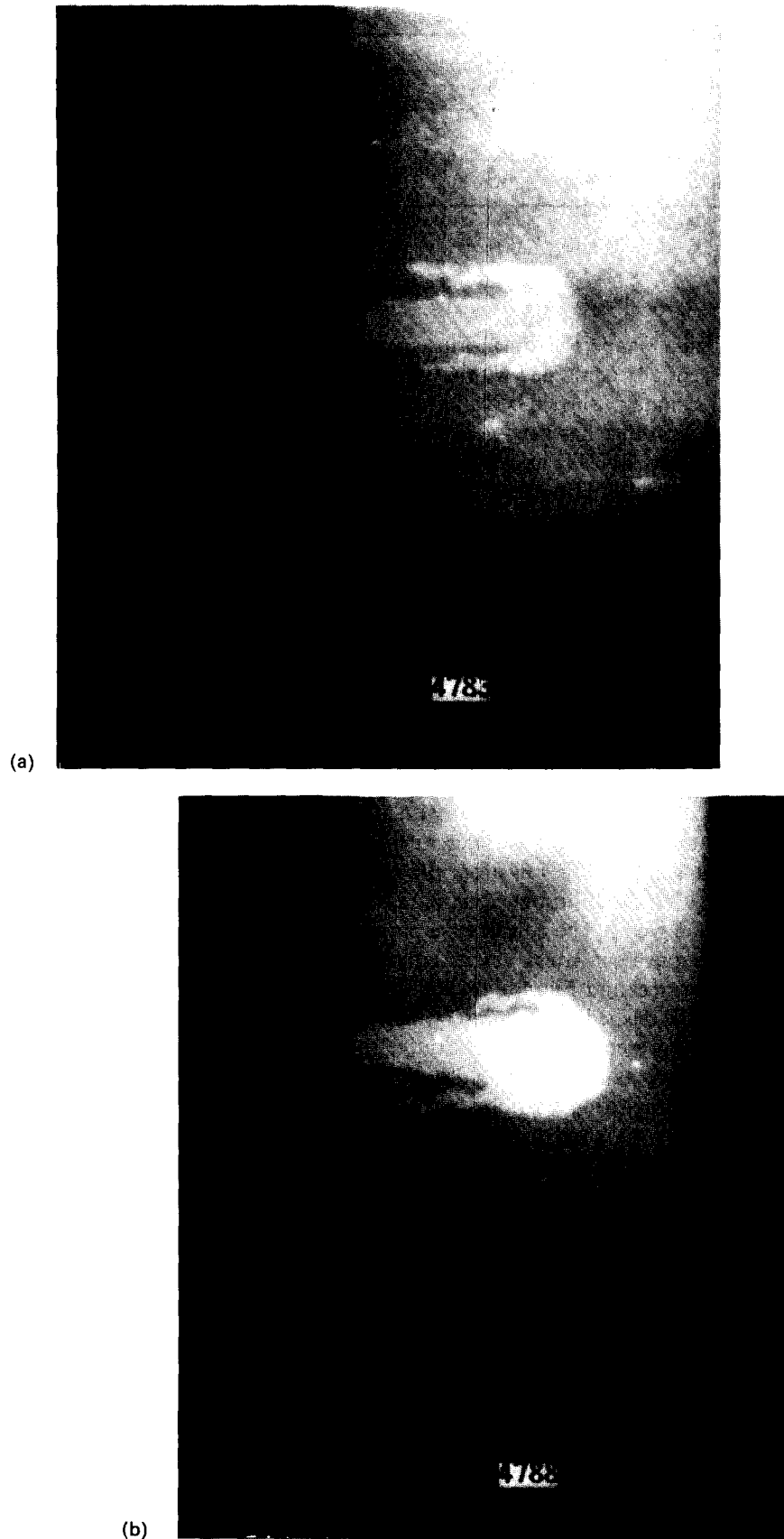


Fig. 3. Flash X-ray of tungsten alloy projectile penetrating a high-hard steel target: (a) $t = 20.7 \mu\text{s}$; (b) $t = 25.3 \mu\text{s}$.

Table 5. Constitutive parameters

	Y_0 (GPa)	B (GPa)	n (—)	C (—)	m (—)	θ_m (K)	G (GPa)	ν (—)	σ_{fail} (GPa)
Tungsten alloy	1.51	0.177	0.12	0.016	1.00	1723	124.0	0.30	2.0
High-hard steel	1.50	0.569	0.22	0.003	1.17	1777	77.3	0.29	2.0
4340 steel	0.792	0.510	0.26	0.014	1.03	1793	77.5	0.29	2.0

$$\sigma_{eq} = (Y_0 + B\epsilon_p^n)[1 + C \ln(\dot{\epsilon}_p/\dot{\epsilon}_0)](1 - \theta^{*m}), \quad \dot{\epsilon}_0 = 1.0 \text{ s}^{-1}, \quad \theta^* = \left(\frac{\theta - \theta_0}{\theta_m - \theta_0} \right), \quad \theta_0 = 300^\circ\text{K}.$$

have a rectangular shape, the dimensions are sufficiently large that the plastic flow of target material is essentially contained within the boundaries of the target. Thus, the assumption of cylindrical symmetry should be valid.† CTH uses a van Leer algorithm for second-order accurate advection that has been generalized to account for a nonuniform and finite grid, and multiple materials; CTH has an advanced material interface algorithm for the treatment of mixed cells. Also, CTH has been modified to allow the flow stress to be a function of strain, strain rate and temperature [6,7]. The thermodynamic treatment of mixed cells used the multiple material pressure and temperature option of CTH. The option used for homogenization of elastic–plastic constants considered only the materials within a mixed cell that could support shear. Square zoning, with 5 zones resolving the projectile radius, was used for the interaction region.

The Johnson–Cook model [8], with parameters for high-hard steel and a tungsten alloy, was used for the computations. The steel used in the experiments had a Vickers hardness of 440, which is approximately $R_c 46$ on the Rockwell C hardness scale. This value is quite close to the hardness of the high-hard steel, $R_c 49$, used to obtain the Johnson–Cook constitutive constants. The Johnson–Cook parameters for the tungsten alloy (7% Ni and 3% Fe) were obtained for a material with a density of 17.0 g/cm^3 . Although the D17.6 alloy used in the experiments is different from that for which the constitutive constants were obtained, small changes in projectile properties have little effect on penetration [3]. Therefore, we used the Johnson–Cook parameters for the numerical simulations, but with a density of 17.6 g/cm^3 . The constitutive parameters used for the calculations are given in Table 5. The equivalent stress versus equivalent plastic strain responses are shown in Fig. 4(a) for the steel and Fig. 4(b) for the tungsten alloy, at two different strain rates (10^0 and 10^5 s^{-1}). The dashed lines represent the response when thermal softening is neglected; the solid lines represent the full constitutive response. For the adiabatic (solid) curves in these figures, it was assumed that 100% of the plastic work goes into heating, i.e. thermal softening. For comparison purposes, the stress–strain curves for 4340 steel, $R_c 30 \pm 2$, are also shown in Fig. 4(a) (and the constitutive constants are given in Table 5). This steel is often used as a surrogate material for rolled homogeneous armor (RHA).

POSITION–TIME, VELOCITY AND LENGTH COMPARISONS

The results of the numerical calculations for the two high-hard steel targets at the two impact velocities are shown as the solid lines in Figs 5 and 6, and the experimental data from Tables 3 and 4 are plotted as circles.‡ Examining the two figures, there exists a slight

† The “targets” for the computations had a larger equivalent radius than the actual targets. Two additional computations were performed to investigate the effect of the lateral boundaries, one each at the two impact velocities. The radius of the cylinder was defined so that the cylindrical target had the same cross-sectional area as the rectangular target. For the 1.25 km/s impact, the computational results did not change. For the 1.70 km/s impact, the projectile went 2.6% deeper, but still did not perforate. All the plastic flow is contained within the actual target at 1.25 km/s ; for the 1.70 km/s impact, the 0.1% plastic strain contour reached the lateral boundary for the smaller diameter target. The results were not affected sufficiently to warrant re-running all the computations.

‡ An error analysis of the experimental data shows that the uncertainties in the data are on the order of the size of the circles.

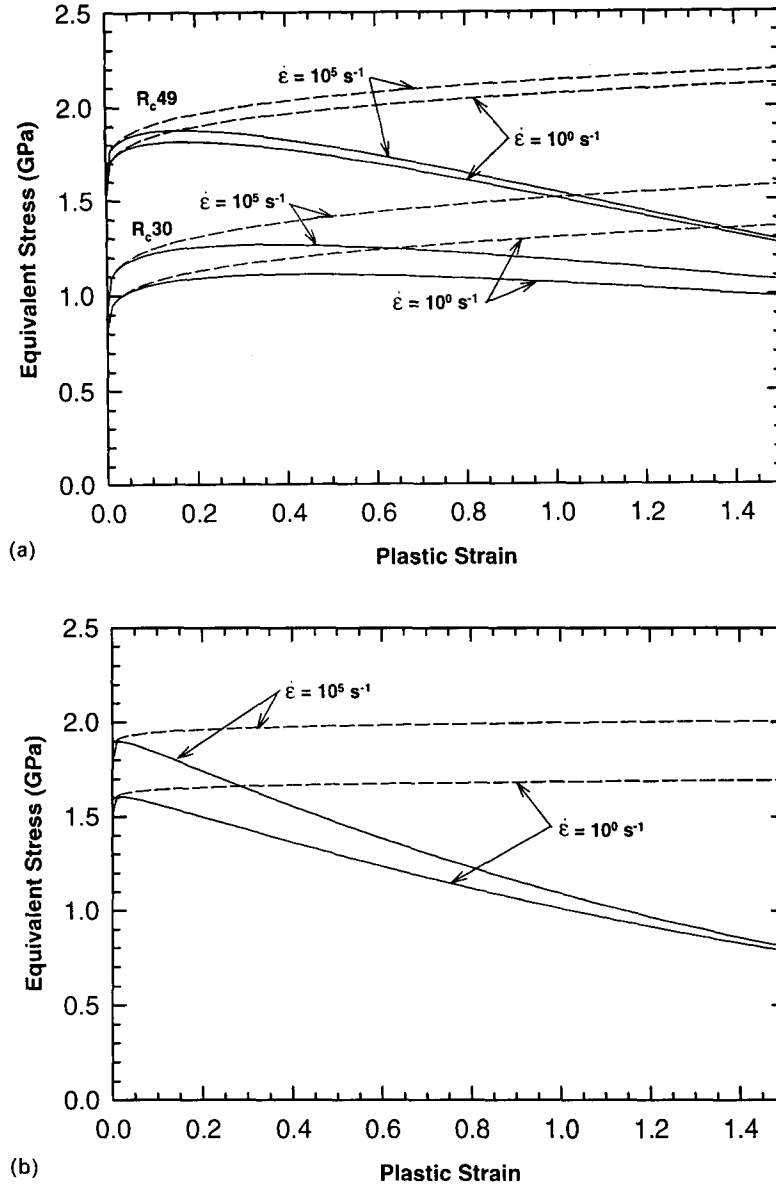


Fig. 4. Equivalent stress versus equivalent plastic strain: (a) high-hard steel and 4340 steel; (b) tungsten alloy.

discrepancy between the computations and the experimental data in the position of the tail of the projectile for the 1.25 km/s impacts (Fig. 5). The computational results indicate that the tail has a velocity that is a little too high (the solid line is above most of the experimental data). However, the positions of the tail for the 1.70 km/s impacts (Fig. 6) appear to be modeled accurately. The tail is decelerated by elastic waves, and the magnitude of the deceleration is directly proportional to the flow stress of the projectile [2,4]. This suggests that a slight change to the constitutive constants for the tungsten alloy would provide better agreement at both velocities. However, the agreement is quite good, particularly since the Johnson–Cook constitutive parameters were obtained for different, albeit similar, materials than were used in the experiments.

A least-squares regression was used to fit cubic polynomials to the positions of the nose and tail as a function of time. The polynomial expressions were then differentiated with respect to time to obtain estimates of the penetration and tail velocities as functions of time. Figure 7 shows the nose and tail velocities for the 1.25 km/s impact case, and Fig. 8

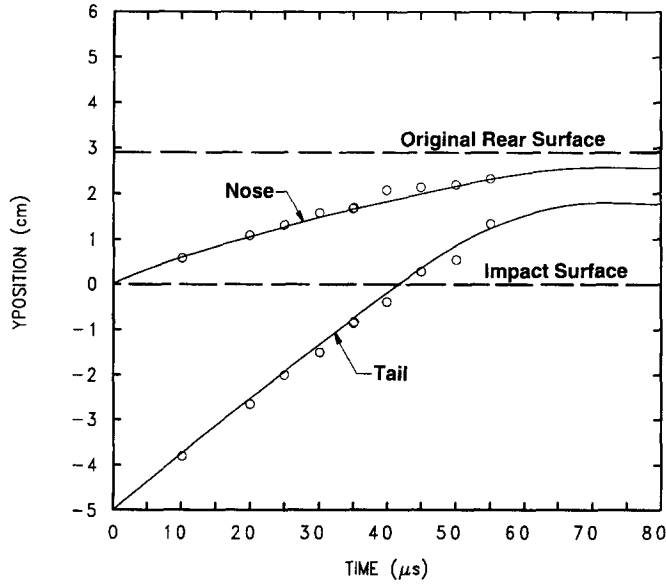


Fig. 5. Projectile nose and tail positions versus time: $V_p = 1.25$ km/s; 2.90 cm thick steel plate.

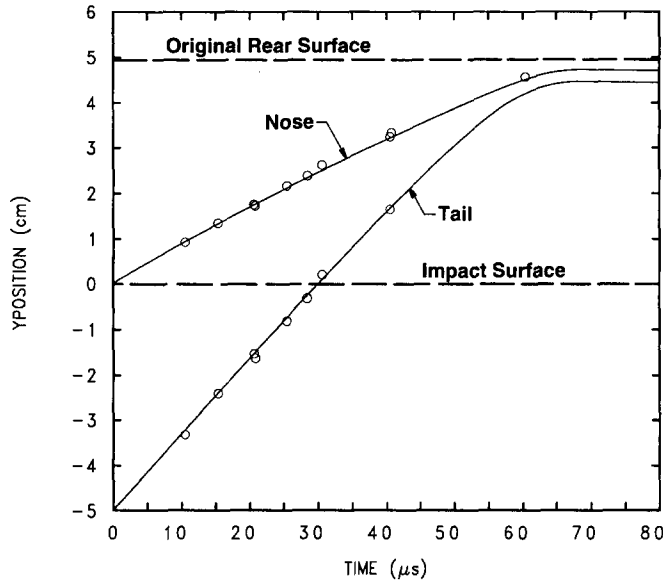


Fig. 6. Projectile nose and tail positions versus time: $V_p = 1.70$ km/s, 4.95 cm thick steel plate.

is the comparable figure for the 1.70 km/s impact case. The solid lines are from the numerical simulations and the dashed lines represent the velocities as inferred from the position–time data. The dashed lines only extend as far in time as the experimental data for each respective curve.

The computational results are in general agreement with the experimentally derived velocities. In Fig. 7, since we know that the impact velocity is initially 1.25 km/s, the difference between the dashed and solid lines for the tail velocity provides an indication of the intrinsic error in estimating the velocities from the experimental data. The simulations are in better agreement with the 1.70 km/s experiments than the 1.25 km/s experiments, consistent with the observations of the position–time data. Lastly, we note that the computations indicate large decelerations of the nose and tail near the end of penetration

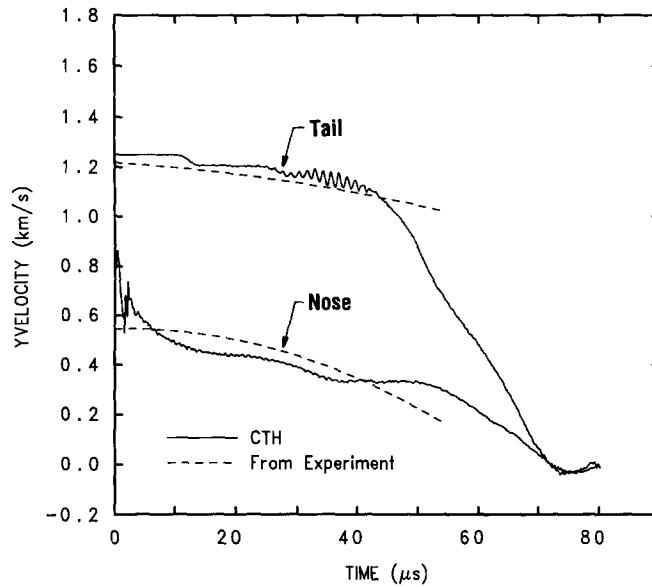


Fig. 7. Projectile nose and tail velocities versus time: $V_p = 1.25$ km/s, 2.90 cm thick steel plate.

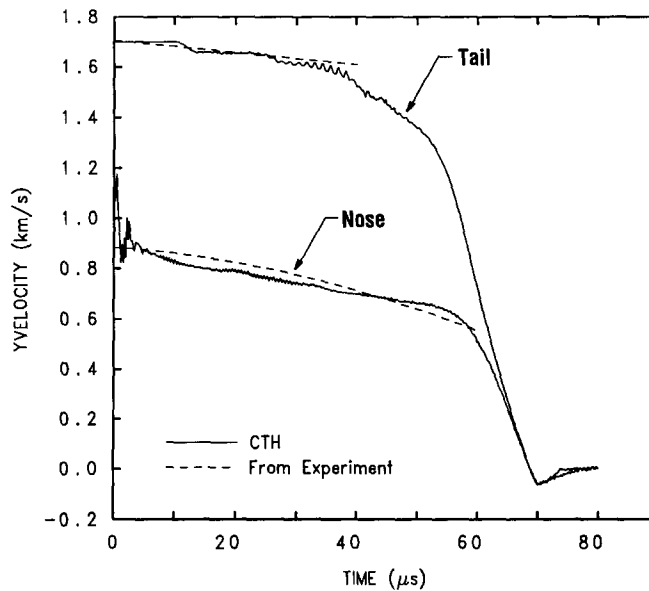


Fig. 8. Projectile nose and tail velocities versus time: $V_p = 1.70$ km/s, 4.95 cm thick steel plate.

which are not observed in the experimentally derived velocities (although there is an indication of this for the nose velocity for the 1.25 km/s case). Insufficient position–time data exist at late times to permit a high-fidelity time derivative, i.e. velocity, at late times.

The measured lengths of the projectiles (Tables 3 and 4), normalized by the projectile diameter, are compared with the calculations in Fig. 9. The computations for the 1.70 km/s impact case (circles) show better agreement with the experimental data than the 1.25 km/s case (squares). This result is expected since the respective projectile tail positions were in better agreement for the 1.70 km/s case. Since the computation indicates the tail is moving a little too fast for the 1.25 km/s case, this computation slightly underpredicts the projectile length, but overall, the agreement between the computations and the experimental results is quite good. Matching experimental data at only one impact velocity can sometimes be

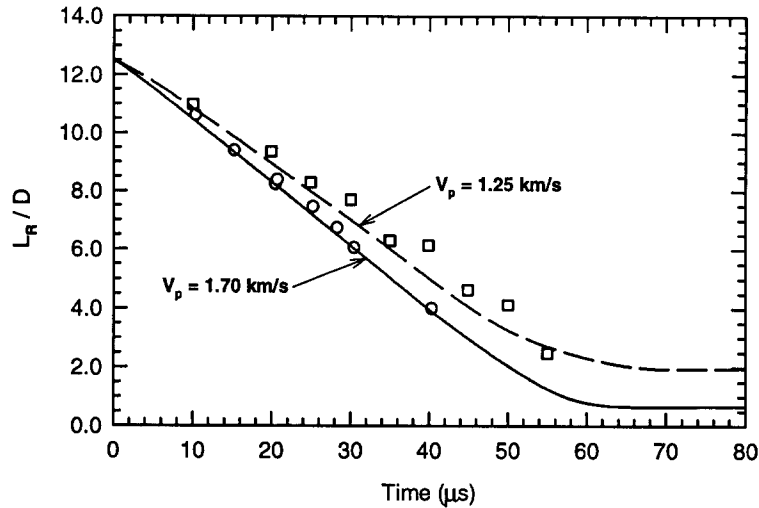


Fig. 9. Normalized projectile length versus time.

fortuitous. However, matching experimental data at more than one impact velocity, using the same constitutive constants, strongly suggests that the overall material behavior is being modeled correctly.[†]

CRATER ANALYSIS

Several of the craters were cross-sectioned and are shown in Fig. 10. The crater diameters for the 1.25 km/s impacts are 0.74 ± 0.02 cm. The impact velocity of 1.260 km/s in test 4811 [Fig. 10(a)] resulted in target perforation, whereas the impact velocity for test number 4812 [Fig. 10(b)] was 1.241 km/s, and the projectile did not perforate the target. Unfortunately, pictures are not available for the 1.70 km/s impacts, but a picture does exist for a similar test, namely 1.68 km/s impact into a 4.85 cm thick target [Fig. 10(c)] (the other targets were 4.95 cm thick). An average crater diameter for this test is 0.83 cm, however, the diameter is larger at the top of the crater (approximately 0.90 cm) and narrows to approximately 0.75 cm deeper in the penetration channel.

The final states of the computations are shown in Fig. 11 (the 1.25 km/s impact into the 2.90 cm thick target) and Fig. 12 (the 1.70 km/s impact into the 4.95 cm thick target). Equivalent plastic strain contours are plotted on the right-hand side of each figure. The final crater, residual projectile and bulging of the back surface of the target for the two target sets are evident. In the computations, the crater has a diameter of approximately 0.69 ± 0.07 cm for the 1.25 km/s impact. This is in good agreement with the experimental observations. At 1.70 km/s, the computations indicate that the crater diameter is slightly larger near the entrance, in agreement with the experimental observations, but the average crater diameter from the computations (approximately 0.67 cm) is 20% smaller than the 0.83 cm observed in the experiment.

Experimentally, the 2.90 and 4.95 cm thicknesses represent the ballistic limit thicknesses at 1.25 km/s and 1.70 km/s, respectively. Therefore, the projectiles should just be perforating the targets in the computations. However, in both cases, the residual projectile has come to rest within the target at a fair distance from the free surface. (Parenthetically, we note

[†] The correct constitutive behavior of the target material is required to match the depth of penetration versus time and L_p versus time data. As a side exercise, simulations were performed for penetration into 4340 steel with a hardness of $R_c 30$, which is lower than that of the actual target material tested. The computational results overpredict the depths of penetration versus time, and the projectiles easily perforated the targets; the residual velocities of the projectiles were approximately 0.91 km/s and 1.22 km/s for the 1.25 km/s and 1.70 km/s impacts, respectively.

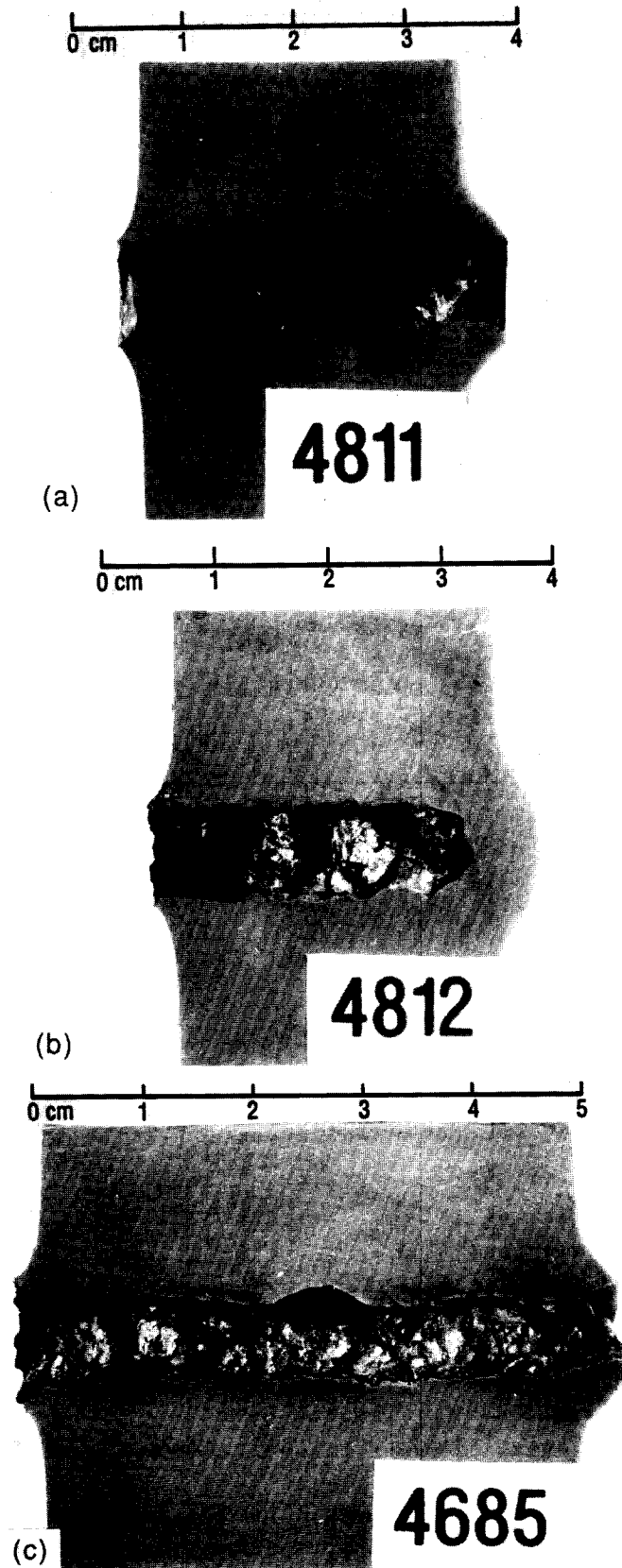


Fig. 10. Cross-sectional views of impact craters: (a) $V_p = 1.26$ km/s, $T = 2.90$ cm; (b) $V_p = 1.24$ km/s, $T = 2.90$ cm; (c) $V_p = 1.68$ km/s, $T = 4.85$ cm.

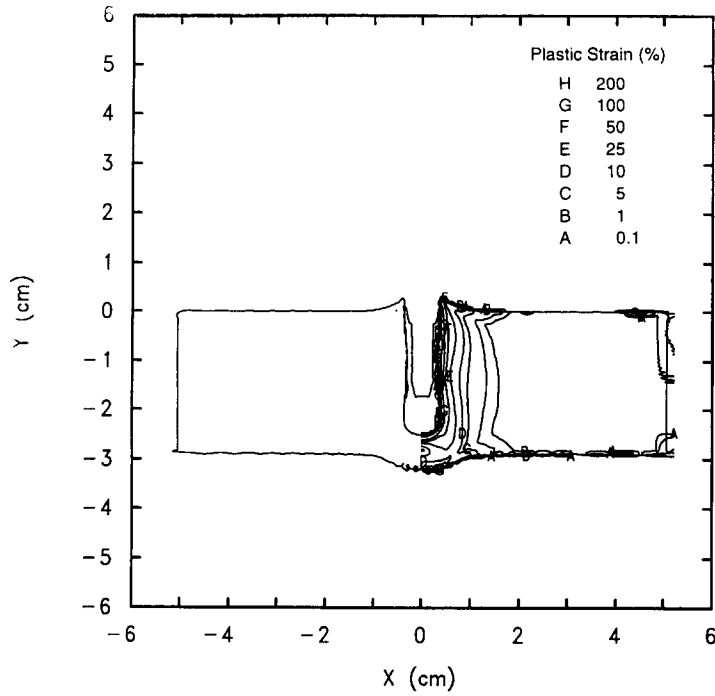


Fig. 11. Material interfaces and equivalent plastic strain: $V_p = 1.25$ km/s, $T = 2.90$ cm, $t = 80$ μ s.

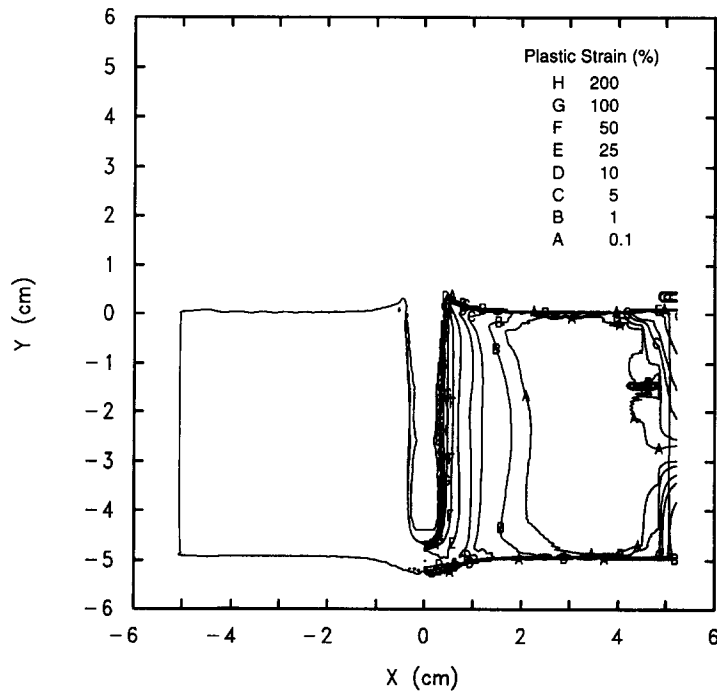


Fig. 12. Material interface and equivalent plastic strain: $V_p = 1.70$ km/s, $T = 4.95$ cm, $t = 80$ μ s.

that the bulge in Fig. 11 looks very similar to the bulge in Fig. 10(b) where the impact velocity was less than the limit velocity.) Thus, although the position–time data from the computations agree quite well with the experimental data, there is considerable question as to whether the computations are reflecting the ballistic limit behavior. In order to examine this question further, the sensitivity of target response and the sensitivity of the numerical simulations near the ballistic limit are explored.

BALLISTIC LIMIT ANALYSIS

One approach for obtaining the ballistic limit velocity is to conduct a series of experiments and measure the residual velocities as a function of the impact velocities. For example, consider experimental data for tungsten alloy projectiles with an initial L/D of ten, impacting two different thicknesses of targets (Fig. 13). (These experiments were also conducted at EMI.) The T/L ratios for the target plates were 0.35 and 0.70. Although two slightly different hardness steels were tested at the T/L ratio of 0.35, differences in the residual velocity cannot be differentiated within the data scatter. The ballistic limit can be estimated from the experimental data by fitting the data to the Lambert equation [9]:

$$V_r = \begin{cases} 0 & 0 \leq V_s \leq V_{BL} \\ a(V_s^p - V_{BL}^p)^{1/p} & V_s > V_{BL} \end{cases} \quad (2)$$

where V_r , V_s and V_{BL} are the residual, striking (impact), and limit velocities, respectively. The slope a , the exponent p , and the limit velocity V_{BL} , are found by performing a nonlinear regression fit to the experimental data. The data in Fig. 13 were fitted to Eqn (2) and the results are shown as the solid lines in the figure. For $T/L = 0.35$, the ballistic limit velocity is 0.982 ± 0.035 km/s; for $T/L = 0.70$, the ballistic limit velocity is 1.373 ± 0.023 km/s. [The uncertainties in the ballistic limit velocities are estimated from the difference between the V_{BL} calculated from Eqn (2) and the impact velocities of the experiments where the projectile did not perforate the target.]

Returning to the tests of Fig. 1, the sensitivity near the ballistic limit can be seen by examining the effect of slight changes in impact velocity (Tables 1 and 2) on the response of the target. The experiments were conducted nominally at the ballistic limit velocity and residual velocity measurements were not made. However, results can be plotted in a different manner. The last columns in Tables 1 and 2 are plotted versus the impact velocity (column 2) in Fig. 14, with the ordinate representing perforation (p); no perforation (np); or p/np ("ideal" ballistic limit damage). The vertical solid lines in Fig. 14 indicate the limit velocities, and the dotted lines show the uncertainties in the limit velocities. The ballistic limit velocity for the 4.95 cm thick target is 1.700 ± 0.010 km/s. This means that, for the extreme cases, there is no perforation at 1.690 km/s, but there is perforation at 1.710 km/s. The limit velocities for a range of target thicknesses have been determined; from these data, the slope of the ballistic limit thickness versus ballistic limit velocity can be computed. $\Delta T_{BL}/\Delta V_{BL} = 0.005$ cm/(m/s) for the steel and projectiles used in the tests of Fig. 1. Thus, the ± 10 m/s uncertainty corresponds to a ΔT_{BL} of ± 0.05 cm. Similar uncertainties (± 10 m/s and ± 0.05 cm for V_{BL} and T_{BL} respectively) exist for the 2.90 cm thick target.

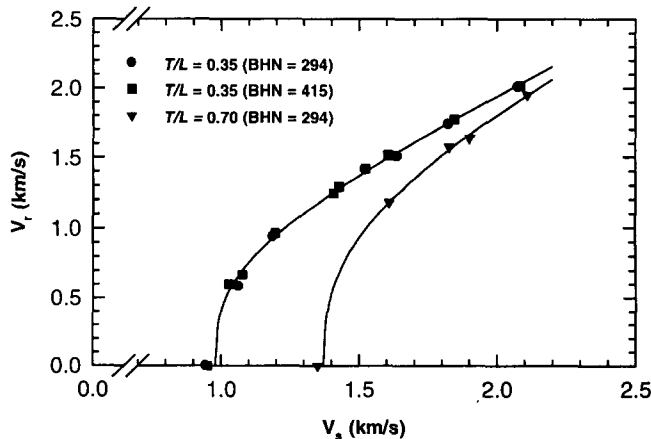


Fig. 13. Residual velocity versus striking velocity.

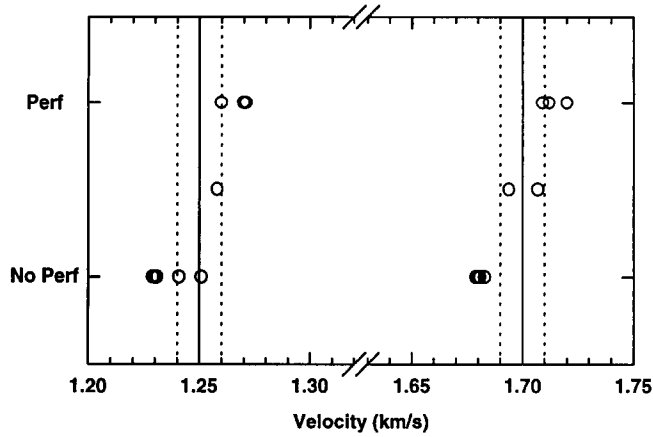


Fig. 14. Target response near the ballistic limit velocities.

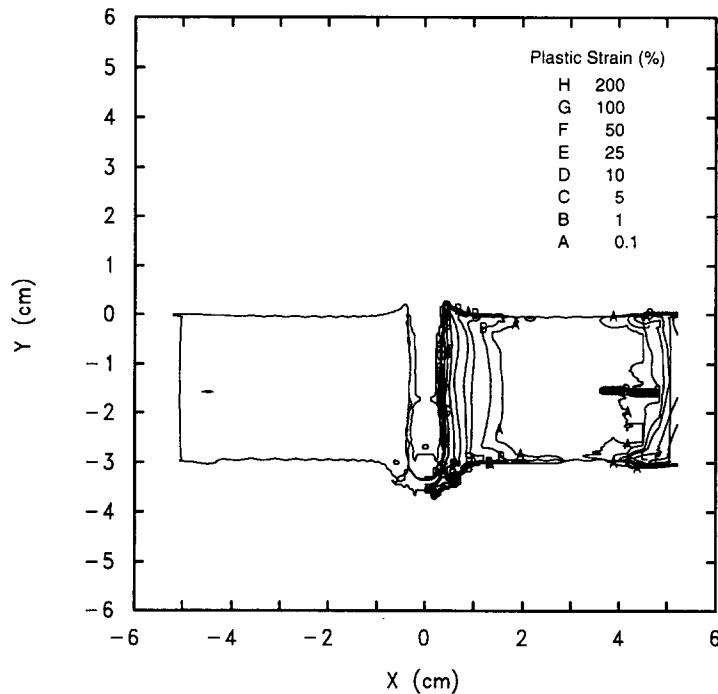


Fig. 15. Material interfaces and equivalent plastic strain: $V_p = 1.30$ km/s, $T = 2.90$ cm, $t = 120$ μ s.

As seen in Fig. 13, large differences in the residual velocity occur for very small changes in the impacting velocity for striking velocities near the ballistic limit velocity. To determine whether the numerical simulations show the same sensitivity as that observed in experiments, additional computations were performed where small changes were made in the striking velocity of the projectile or the thickness of the plate, or both, and the subsequent effects on the projectile-target response were observed.

The first set of excursions examined the effect of increasing the impacting velocity by 0.05 km/s. Figure 15 shows that at 1.30 km/s, the 2.90 cm thick target is perforated. A plug has formed in the target, with a crack starting at the crater radius and running at approximately 45° to the back surface of the target. The residual velocity of the remnant projectile and plug is approximately 0.025 km/s. A similar computation was performed on the 4.95 cm thick plate (Fig. 16). At an impact velocity of 1.75 km/s, the projectile still has not perforated the target, although the presence of a significant amount of void in the neck

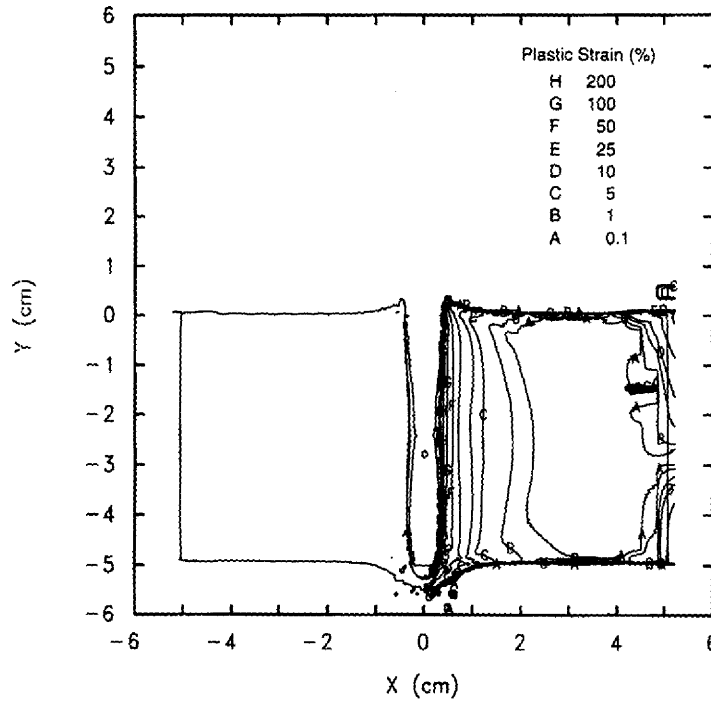


Fig. 16. Material interfaces and equivalent plastic strain: $V_p = 1.75$ km/s, $T = 4.95$ cm, $t = 80$ μ s.

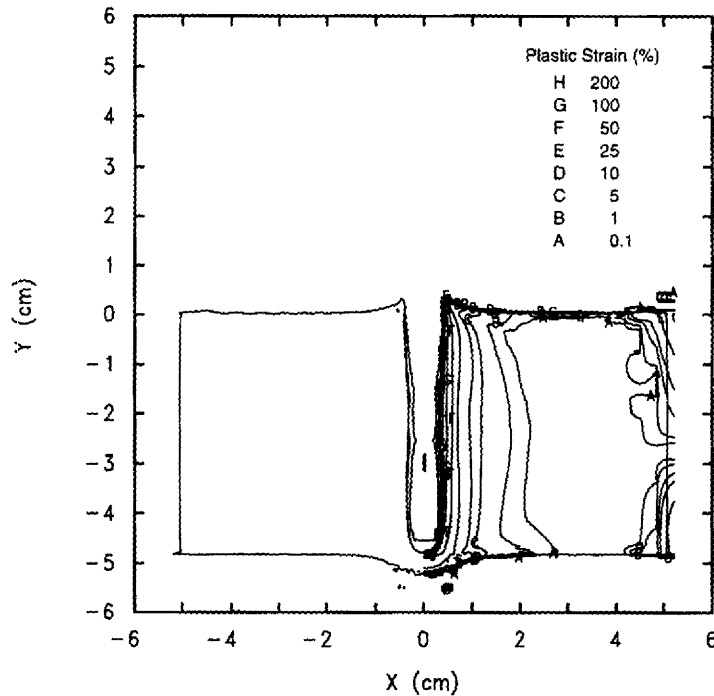


Fig. 17. Material interfaces and equivalent plastic strain: $V_p = 1.70$ km/s, $T = 4.85$ cm, $t = 80$ μ s.

of the bulge, which can be seen in the left-hand side of the figure, indicates that total plug formation has almost occurred. Additionally, equivalent plastic strains of more than 50% have accumulated in the neck region of the bulge.

Instead of increasing the penetration velocity further for the 4.95 cm thick plate, it was decided to decrease the plate thickness by 0.1 cm. Computations were performed at impact velocities of 1.70 km/s and 1.75 km/s (Figs 17 and 18). At 1.70 km/s, the projectile is stopped

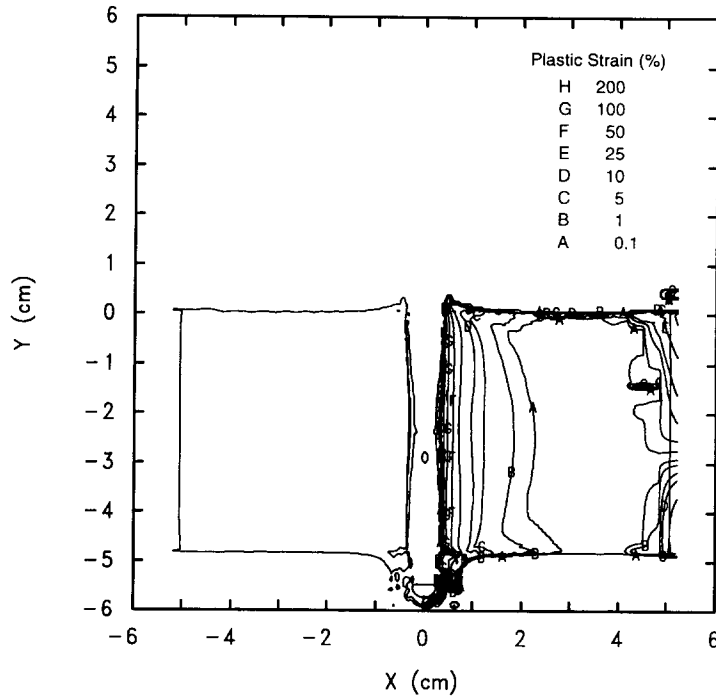


Fig. 18. Material interfaces and equivalent plastic strain: $V_p = 1.75$ km/s, $T = 4.85$ cm, $t = 80$ μ s.

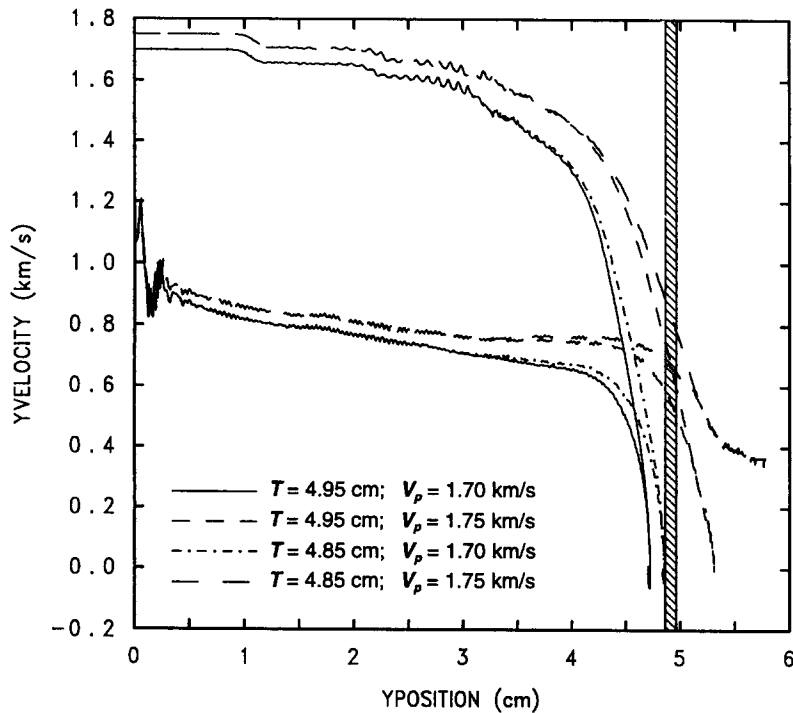


Fig. 19. Penetration and tail velocities versus depth of penetration.

by the plate, although there are 25%–50% plastic strains in the neck region of the bulge. At 1.75 km/s (Fig. 18), the target is perforated and the projectile has a residual velocity of approximately 0.37 km/s. Therefore, for a 0.05 km/s increase in the impacting velocity, the projectile went from nonperforating to perforating with a residual velocity of 0.37 km/s. The results of the four computations are summarized in Fig. 19, where the projectile tail

and nose velocities are plotted as a function of the penetration depth. The original thicknesses (before bulging of the target) of the two targets are shown in the figure. The overall response is very similar to that observed in Fig. 13, that is, the computations show a strong sensitivity to initial conditions near the ballistic limit. In this way, the computations are displaying the expected qualitative behavior near the ballistic limit.

TARGET FAILURE

Although the computations display the correct qualitative behavior, they do not reproduce the ballistic limit within the experimental uncertainties. The most probable reason for this is an inadequate treatment of target failure. For example, armor steels have a tendency to form shear bands [1,10,11]; these shear bands lower the ballistic limit velocity for a given target thickness or increase the ballistic limit thickness for a specific impact velocity. Shear bands are a very localized phenomena and have proven to be difficult to simulate, one main reason being the relatively large zone sizes required to perform multidimensional simulations. Due to the inability to model complicated material failure, breakout is not modeled particularly well computationally [12,13] (Ref. [13] describes the need for more realistic failure criterion). In the calculations reported here, fracture is simulated by inserting void volume into a computational cell when the maximum tensile stress exceeds a tensile criterion. The void volume results in a reduction in stress of the solid material(s) within the computational cell so that the failure criterion is not exceeded. (The values for the fracture stresses used in the present computations are given in Table 5.) For computational purposes, the void is treated as an additional material. As more void is inserted in a region to prevent excessive tensile stresses, it can appear that voids are coalescing to form fracture surfaces. Although not studied rigorously, this process is, however, probably sensitive to zoning.

Even though the failure mechanisms are not being modeled explicitly, the algorithm described above appears to capture the essence of some types of fracture processes. As evidence of this, the numerical simulations do qualitatively reproduce the experimentally observed behavior near the ballistic limit since small changes in the initial conditions produce relatively large changes in the response. Although more work needs to be performed to simulate the breakout stage more accurately, we conclude that agreement between the computations and experiments is encouraging.

One last series of computations used the Johnson–Cook damage model [8]; this model is considerably different than the void insertion model. The Johnson–Cook damage model is effectively a strain-to-failure model in which the failure strain is a function of strain rate, the ratio of mean stress to von Mises equivalent stress, and temperature. For the conditions in this study, the strain-to-failure varied between 25% and 100%, but, in general, was of the order of 50%. Upon failure, the material cannot support shear or tensile stresses. For both impact cases, the computations tended to overpredict the depths of penetration as a function of time, and the targets were perforated; the residual velocity was approximately 0.80 km/s for the 1.25 km/s impact case, and approximately 0.90 km/s for the 1.70 km/s impact case. Crater diameters were wider, and the impact produced more “debris” than observed in the experiments. In summary, when compared with the experimental data, the computational results using the Johnson–Cook damage model were not as satisfactory or as accurate as the void insertion model, but neither model provides an accurate description of material behavior near the ballistic limit condition.

SUMMARY

It has been demonstrated in previous studies that numerical simulations of eroding projectiles impacting thick targets can match the final depth of penetration. Although the depth of penetration is important, it is not the only factor of interest in modeling the penetration process. The constitutive behavior of metals is sufficiently mature so that calculated penetration–time behaviour is in good agreement with time-resolved experimental

data. On the other hand, computational modeling of failure is not as well developed. Pioneering work in failure modeling has been performed by some researchers, notably Curran, Seaman and Shockey of SRI International [11,1]. Their approach has been to develop micromechanical models of failure, but these models have not been incorporated into general release hydrocodes because of the burden they place on computational resources and the difficulty in determining the micromechanical material damage constants. Failure modeling is also made difficult by the various modes of failure. For example, Ravid and Bodner have used experimental observations to pose at least three different failure modes that can be operative in ballistic limit testing [14]. With possible geometrical variations within the various failure modes. Ravid and Bodner have a total of eight different types of target plugs that can be ejected. In their work, the failure mode must be selected *a priori* (based on experience); that is, there is no reliable analytical means to select which failure mode is the operative mode for a particular test. Thus, although the next logical step to improve the capabilities of numerical simulations is the development and incorporation of robust and efficient algorithms for the initiation, growth and propagation of failure, this promises to be a difficult task.

Acknowledgements—A portion of this work was supported under contract DAAL03-92-K-0001, administered by the U.S. Army Research Office. The authors would like to thank Mr Dick Sharron for his support in performing some of the CTH calculations. We also would like to thank Professor Sol Bodner for his helpful comments on drafts of this paper. The authors gratefully thank Ms Janet Banda for her assistance with the preparation of the manuscript. Lastly, the authors are appreciative of the insightful comments and suggestions of one of the reviews; we feel that the final manuscript has been improved as a result.

REFERENCES

1. C. E. Anderson, Jr and S. R. Bodner, Ballistic impact: the status of analytical and numerical modeling. *Int. J. Impact Engng* **7**(1), 9–35 (1988).
2. C. E. Anderson, Jr and J. D. Walker, An examination of long-rod penetration. *Int. J. Impact Engng* **11**(4), 481–501 (1991).
3. C. E. Anderson, Jr, J. D. Walker and G. E. Hauver, Target resistance for long-rod penetration into semi-infinite targets. *Nucl. Engng Design* **138**, 93–104 (1992).
4. A. Tate, Long rod penetration models—part II. Extensions to the hydrodynamic theory of penetration. *Int. J. Engng Sci.* **28**, 599–612 (1986).
5. J. M. McGlaun, S. L. Thompson and M. G. Elrick, CTH: a three-dimensional shock wave physics code. *Int. J. Impact Engng* **10**(1–4), 351–360 (1990).
6. W. W. Predebon, C. E. Anderson, Jr and J. D. Walker, Inclusion of evolutionary damage measures in Eulerian wavecodes. *Comp. Mech.* **7**(4), 221–236 (1991).
7. S. Silling, Stability and accuracy of differencing methods for viscoplastic models in wavecodes. *J. Comp Phys.* **104**, 30–40 (1993).
8. G. R. Johnson and W. H. Cook. Fracture characteristics of three metals subjected to various strains, strain rates, temperatures and pressures. *Engng Fract. Mech.* **21**(1), 31–48 (1985).
9. J. A. Zukas, T. Nicholas, H. G. Swift, L. B. Greszczuk and D. R. Curran, *Impact Dynamics*, Chapter 5. Wiley, New York (1982).
10. M. Raftenberg, Lagrangian hydrocode simulations of rolled-homogeneous-armor plate perforation by a shaped charge jet. *Int. J. Impact Engng* in publication (1994).
11. D. R. Curran, L. Seaman and D. A. Shockey, Dynamic failure of solids. *Physics Reports* **147**(5 and 6), 254–388 (1987).
12. C. E. Anderson, Jr, S. A. Mullin and C. J. Kuhlman, Computer simulation of strain-rate effects in replica scale model penetration experiments. *Int. J. Impact Engng* **13**(1), 35–52 (1993).
13. J. E. Reaugh, The influence of the target strength model on computed perforation. *Joint AIRAPT/APS Conf. High Pressure Sci. Tech.* Colorado Springs, CO (1993).
14. M. Ravid and S. R. Bodner, Dynamic perforation of viscoplastic plates by rigid projectiles. *Int. J. Engng Sci.* **21**(6), 577–591 (1983).